Journal of Catalysis **211,** 335–346 (2002)
doi:10.1006/jcat.2002.3699

Effect of Support on the Size and Composition of Highly Dispersed Pt–Sn Particles

L. Bednarova,* C. E. Lyman,† E. Rytter,*,‡ and A. Holmen*,[1]

*Department of Chemical Engineering, Norwegian University of Science and Technology, N-7491 Trondheim, Norway; †Lehigh University, Whitaker Laboratory, Bethlehem, Pennsylvania 18015; and ‡Statoil Research Center, N-7005 Trondheim, Norway

Received February 20, 2002; revised May 28, 2002; accepted May 28, 2002

Platinum and tin deposited on γ-Al_2O_3, MgO, and Mg(Al)O supports were investigated by CO chemisorption and analytical electron microscopy in the scanning transmission electron microscopy with energy-dispersive X-ray spectrometry (STEM/EDX). Composition and size of individual particles in the 1-nm range are presented and results are compared with dispersion measurements obtained from volumetric chemisorption. We demonstrate that dispersion determined by chemisorption measurements can give unrealistically low values, possibly caused by metal–support interaction, while STEM/EDX reveals the correct size of metal particles. The metal–support interaction seems not to be present on γ-Al_2O_3 support but only on Mg(Al)O and MgO supports. The performance of the catalyst in propane dehydrogenation is related to the amount of Pt on the metal particle surface. It is shown that there is a relationship between the composition of metal particles and the activity of the catalyst. The most active is a catalyst that contains metal particles with high Pt content; however, some Sn is necessary for reduced coking and probably for increased stability.

Key Words: **Pt–Sn catalysts; Mg(Al)O; Al_2O_3; MgO; Pt–Sn particle composition–size diagram; analytical electron microscopy; X-ray spectrometry; metal–support interaction; propane dehydrogenation.**

INTRODUCTION

Catalytic dehydrogenation of light alkanes is an important industrial process with potential for improvement. Nobel metals, especially platinum, are key ingredients in most dehydrogenation catalysts. It has become a common practice to incorporate a second metal into the catalyst (Sn, Ag, Ge, Pb) (1–5) and/or add alkali metals (1–3). There have been numerous studies on the effect of Sn in Pt–Sn catalysts, but this is still not completely understood (6, 7). The promotion of monometallic Pt catalysts by Sn has several advantages: it prevents the hydrogenolytic effect of platinum, favors the selectivity of the dehydrogenation reactions, mitigates the sintering effect, and decreases the deactivation rate caused by carbon formation. Contradictory results have been reported in the literature concerning the state of Sn. Some studies suggest that Sn is not reduced to zero valency (8); in other cases, at least part of the Sn was found to be present as Sn^0 after reduction (9, 10). It also has been reported that intermetallic Pt–Sn particles are present (10, 11). The state of Sn depends on catalyst preparation, metal loadings and Pt : Sn ratio, support material, and pretreatment procedures; therefore, contradictory results are not surprising. Moreover, Chojnacki and Schmidt (12) found on Pt–Sn/SiO_2 with 2- to 20-nm particles that Pt and Sn atoms within a single particle do not necessarily form a uniform distribution. It also has been reported that the metal particles contain less tin than is present over the entire bulk catalyst (8, 13). It was suggested that the remaining tin is probably in a highly dispersed state.

The dehydrogenation reactions proceed on small ensembles of surface platinum atoms (14) while hydrogenolysis, isomerization, and coking proceed through the formation of highly dehydrogenated species over multiple adsorption sites. Support materials can modify the selectivity by catalyzing the lateral reactions, but they can also influence the properties of the final metallic phase. The standard supports that are usually used are γ-Al_2O_3 and SiO_2; however, nonacidic supports result in less cracking, fewer polymerization reactions, and remarkable stability. Magnesium aluminate ($MgAl_2O_4$) has been extensively studied recently (15–17) and is used in the *Phillips Star* process for dehydrogenation of low-molecular-weight paraffins (18).

A newly developed atomic-resolution *in situ* transmission electron microscopy (TEM) (19) can give insight into the location and state of promoter under the reaction conditions and, therefore, give better understanding of the influence of the promoter on the catalytic activity. Analytical electron microscopy—scanning transmission electron microscopy combined with microanalysis by energy-dispersive X-ray spectrometry—has also proved to be a powerful technique for studying highly dispersed bimetallic systems, providing detailed metal particle size and composition information (20, 21). However, detection of metallic tin species is very difficult due to the lower electron scattering cross section of

[1] To whom correspondence should be addressed. Fax: +47 73 595047. E-mail: holmen@chemeng.ntnu.no.

0021-9517/02 $35.00

Sn compared to that of Pt, making the Sn-rich particles almost indistinguishable from the support. There are several studies of Pt–Sn catalysts (8, 16, 22–24), but none of them reports detailed compositions of individual metal particles in the range of 1 nm. However, this is the particle size that is required for industrial catalysts; therefore, investigation of such highly dispersed catalysts is important.

In this work, we have compared Pt–Sn catalysts supported on γ-Al_2O_3, MgO, and Mg(Al)O. The coexistence of different bimetallic phases in the catalyst makes it difficult to interpret data from conventional bulk characterization methods such as temperature-programmed reduction (TPR) or chemisorption. We characterized the catalysts with the highest resolution analytical electron microscope available, which provided direct evidence of the compositions of individual metal particles as small as 0.5 nm (few tens of atoms). Furthermore, we correlated the data with volumetric chemisorption results to show that chemisorption can be suppressed due to metal–support interactions. Catalyst performance in propane dehydrogenation was used to demonstrate that not only metal particle size but also the compositions of individual particles are important for this reaction.

EXPERIMENTAL

Catalysts

All samples were prepared by impregnation. A γ-Al_2O_3 ($S_{BET} = 308$ m^2/g) support material from Kaiser Chemicals and MgO ($S_{BET} = 71$ m^2/g) support from Engelhard Industries were dried in air for 12 h at 120°C. Supports were impregnated to incipient wetness with Sn, using $SnCl_2 \cdot 2H_2O$ (Merck, 98–100%) and distilled water as solvent, dried in air at 110°C for 12 h, and wet calcined at 550°C for 2.5 h, followed by 2 h of calcination in dry air at the same temperature. The purpose of the wet calcination was to remove Cl left by the metal salt. Platinum impregnation to incipient wetness with $H_2PtCl_6 \cdot 6H_2O$ (J. T. Baker; assay, 37.50% Pt) using distilled water as solvent was followed by drying, wet calcination, and dry calcination under the same conditions as for the Sn impregnation step. Platinum and tin contents were measured by atomic absorption spectrometry (AAS), which confirmed that neither metal was lost during the preparation. The metal contents of the completed specimens were 0.4 wt% Pt–1.3 wt% Sn/γ-Al_2O_3 (sample ALU) and 1.0 wt% Pt–1.3 wt% Sn/MgO (sample MGO). Both samples contained low amounts of chlorine, below the amount detectable by ion chromatography (0.2 wt%). A third sample on a calcined hydrotalcite, 0.3 wt% Pt–1.3 wt% Sn/Mg(Al)O (sample HT1), was obtained from SINTEF, Oslo, Norway. In this sample, platinum and tin were impregnated on a form of Mg(Al)O obtained by calcining hydrotalcite (Mg/Al $\sim$ 2.4) according to published procedures (25, 26). The aluminum atoms are used to stabilize the support surface area at higher temperatures (27). Samples examined in a dedicated scanning transmission electron microscope were in the fresh state or after reduction in hydrogen for 2 h at 600°C (samples labeled F and R, Table 1).

Volumetric Chemisorption

Volumetric chemisorption of CO was measured at 35°C using a Micromeritics ASAP2010 Chemi instrument. Samples were heated and reduced in hydrogen at 600°C for 2 h and analyzed. The values reported are related to the difference between two isotherms with an intermediate evacuation down to 10^{-5} bar in between for 30 min. It can be assumed that the adsorption stoichiometry of CO/Pt is close to 1. It was verified that pure Sn does not chemisorb CO at 35°C. We refer to this measured dispersion as "chemisorption dispersion."

Analytical Electron Microscopy

The specimens were examined in a dedicated scanning transmission electron microscope (STEM) (VG HB-603) equipped with an energy-dispersive spectrometer (EDX) system employing a windowless Si(Li) detector (Oxford Instruments model eXL) (28). The instrument was operated

TABLE 1

Description of Samples

Sample	Support material	Bulk overall catalyst composition: Nominal content of Pt (wt%)	Bulk overall catalyst composition: Nominal content of Sn (wt%)	Bulk overall catalyst composition: Pt/Sn atomic ratio	Pt content in particles (wt%): From nominal content	Pt content in particles (wt%): From EDX anal.	Treatment before analysis in STEM
ALU_F	γ-Al_2O_3	0.4	1.3	1 : 3.5	22	38	None (F)
ALU_R						46	Reduction (R)
MGO_F	MgO	1.0	1.3	1 : 1.3	44	48	None (F)
MGO_R						57	Reduction (R)
HT1_F	Mg(Al)O	0.3	1.3	1 : 4.9	17	37	None (F)
HT1_R						68	Reduction (R)

at 300 kV. Quantitative X-ray analysis of bimetallic nanoparticles smaller than 5 nm requires a dedicated STEM/EDX instrument with a cold-field emission electron source, a gun lens, and an energy-dispersive X-ray detector with a collection angle greater than about 0.1 steradians. Such an instrument has been used to develop composition–size diagrams for Pt–Rh (21) and Pt–Re (20) bimetallic catalysts and is used in this study.

Specimens were prepared for analysis by crushing the catalyst material in a mortar and pestle and dry dispersing the finest of the resulting shards on holey carbon films supported on Ti grids. For each examination a new specimen was prepared and inserted into the microscope vacuum approximately 15 h before analysis to remove volatile species. Images were obtained with the annular dark-field detector (ADF), generally at magnifications of 2–5 Mx. The metal particle size was determined by measuring with a ruler on a stored digital image. The error in measuring the particle size was estimated to be ± 0.2 nm. Shards of catalyst about 0.5–1 μm were analyzed, as smaller ones were unstable on the carbon film or broke easily into smaller pieces under the beam. The analysis of metal particles was performed only for particles on thin layers of support at the edges of catalyst shards.

Metal particles were analyzed by EDX either in "spot mode" or "reduced area mode," depending on metal particle size, thickness of support, and distance from other metal particles. Spot mode was used for larger metal particles, metal particles on thicker pieces of support, or when metal particles were close to one another; in other cases reduced area mode was used. Examples of collected EDX-spectra from single metal particles on the ALU_R sample are shown in Fig. 1. Figure 1c shows a spectrum from a 3-nm Pt–Sn particle and a second spectrum from a region of the support 15 nm away. Note that the spectrum from the support shows no evidence of Pt and only the slightest suggestion of Sn. Thus, X-rays from metal particles can legitimately by used to produce quantitative analyses. It was possible to distinguish in the ADF image between Pt-rich and Sn-rich particles: Pt-rich particles have high contrast and sharp particle boundaries in annular dark-field images, whereas Sn-rich particles have lower visibility and look more like blurry patches with diffuse boundaries (Fig. 2). The smallest detected particles were about 0.5 nm. For reliable analysis (29) at least 400 counts had to be collected in the PtL(summed PtL_α and PtL_β lines) and SnL (unresolved SnL_α and SnL_β lines) peaks so that the relative counting error in a single measurement was under 15%. About 30,000 counts in PtL and SnL were accumulated for larger particles, which corresponds to a counting error of 2%. To produce a meaningful composition–size diagram it was necessary to collect data from about 100 particles on each sample. All EDX spectra were processed with Desktop Spectrum Analyzer (DTSA) software produced by the National Institute of Standards and Technology (NIST) (30). The Simplex procedure, which uses digital filtering, was applied to remove the background intensity under the X-ray peaks.

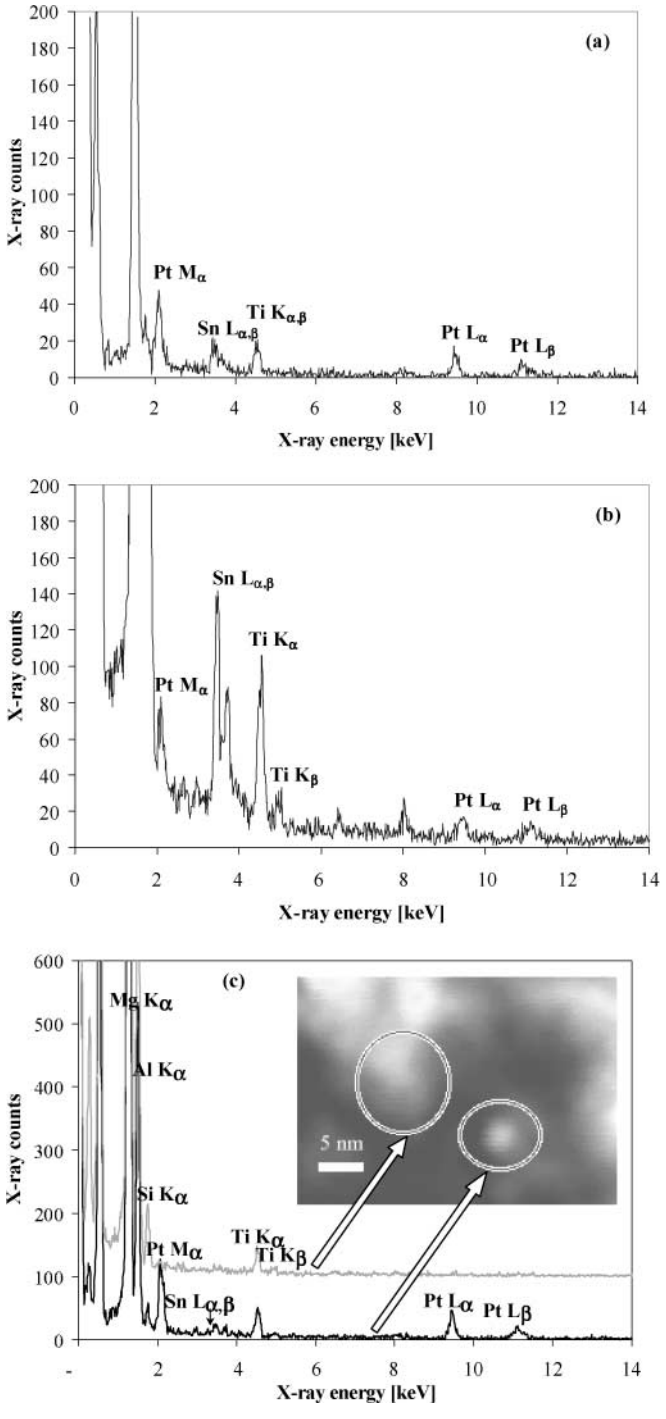

FIG. 1. (a) X-ray spectrum from a 0.5-nm Pt–Sn particle in sample ALU_R. (b) X-ray spectrum from a 3.0-nm Pt–Sn particle in sample ALU_R. (c) X-ray spectrum from a Pt–Sn particle and support proving that the support contains no metal (Pt or Sn) 15 nm from a metal particle.

A Cliff–Lorimer equation (31) relates the mass fraction of Pt and Sn to the number of counts in the L-series peaks,

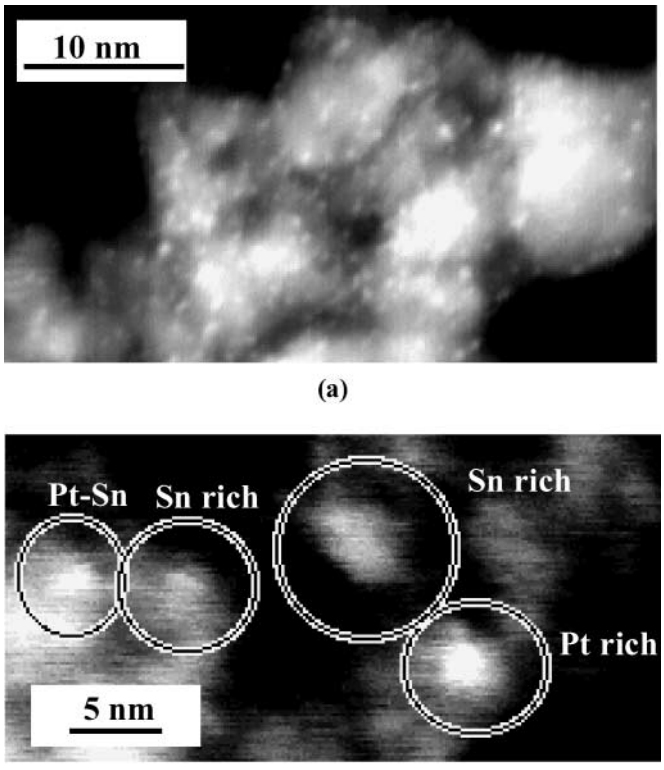

FIG. 2. Examples of annular dark-field (ADF) images of Pt–Sn particles. (a) Bright 1-nm-diameter Pt–Sn particles on MgO support (sample MGO_R). (b) Pt-rich and Sn-rich particles in sample HT1_F.

PtL and SnL,

$$\frac{c_{Pt}}{c_{Sn}} = k\frac{I_{Pt}}{I_{Sn}}, \qquad [1.1]$$

where c is the mass fraction, I is net X-ray intensity, and k is the Cliff–Lorimer k-factor. X-ray absorption and fluorescence effects were considered negligible in these small particles. The weight fractions of Pt and Sn in all presented results are based on

$$c_{Pt} + c_{Sn} = 1, \qquad [1.2]$$

assuming only Pt and Sn exist within the metal particle. If we substitute Eq. [1.2] into Eq. [1.1] and rearrange it, we can write as follows:

$$c_{Pt} = k\frac{I_{Pt}}{I_{Sn} + k.I_{Pt}}. \qquad [1.3]$$

A suitable Pt–Sn standard was not available, so the k-factor was calculated (32) for 300-kV accelerating voltage to be 1.4 ± 0.3, with the error estimated according to Wood *et al.* (33). The k-factor does not dramatically influence the calculated composition of the particle. For instance, a particle that contains 72 wt% Pt using k-factor 1.4 would have composition of 76 wt% Pt with k-factor 1.7, and 67 wt% Pt for k-factor 1.1. This means that the composition of metal particles is within ±5 wt% accuracy in the composition–size diagrams presented under Results.

Calculation of Pt Dispersion

An estimate of metal particle dispersion was calculated from the size (ADF image) and composition (EDX analysis) of each individual metal particle in a sampled population of about 100 particles. Two methods were used.

(a) Pt–Sn intermetallic phases. It was assumed that equilibrium was reached for the metal particles and that the phase diagram could be applied. Each of the metal particles was assigned a phase from the phase diagram corresponding to its composition measured by EDX. A series of Pt, Pt_3Sn, PtSn, Pt_2Sn_3, $PtSn_2$, and $PtSn_4$ spherical particles, with diameters corresponding to individual particles found on the samples, was generated using the program ATOMS (34). The surface energy of platinum is greater than tin; thus platinum was used as the center atom of the particles. If tin had been used as the center atom, the dispersion would have been about the same for particles larger than about 1.5 nm.

(b) Pt(fcc) structure. It was assumed that all particles have the (fcc) structure and that some Pt atoms are replaced by Sn atoms. A series of spherical particles, with diameters corresponding to individual particles found on the samples, was generated using the program ATOMS (34).

The number of platinum atoms and surface platinum atoms were counted manually for each simulated particle by displaying it in 3-D. The program ATOMS does not allow the user to relax the atomic configurations in the particles; however, we believe that the error this causes in the number of surface atoms is negligible. A 0.8-nm Pt particle generated by the program ATOMS was compared with a particle of the same size in a fully relaxed structure (33). The number of platinum surface atoms did not change, and therefore, the same number of molecules could be adsorbed on both relaxed and unrelaxed particles (Fig. 3). The number of platinum atoms in a particle obtained from ATOMS was corrected by the actual composition of the metal particle. This means that for the first method, where we assume metal particles have the structures of various Pt–Sn intermetallic compounds, a certain number of Pt atoms in the particle was exchanged for Sn atoms or some Sn atoms were exchanged for Pt atoms so that the composition of the generated particle was the same as the composition of the metal particle obtained by EDX. For instance, if there was a 2-nm metal particle on the sample that was measured to be 58 wt% Pt (46 at% Pt), it would be closest to the Pt_2Sn_3 structure, according to the phase diagram. Program ATOMS calculated that a 2-nm particle with the Pt_2Sn_3 structure would contain 195 atoms with 72 Pt atoms, of which 35 are Pt surface atoms. The composition of this generated particle is 37 at% Pt, and therefore, we exchanged 18 Sn atoms

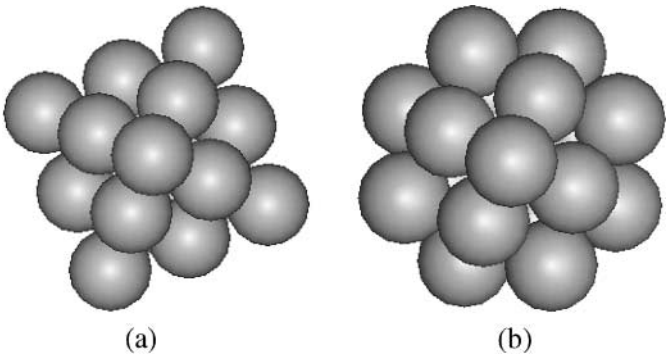

FIG. 3. Generated Pt particle of 19 atoms: (a) from ATOMS, not relaxed; (b) relaxed in its global minimum (35).

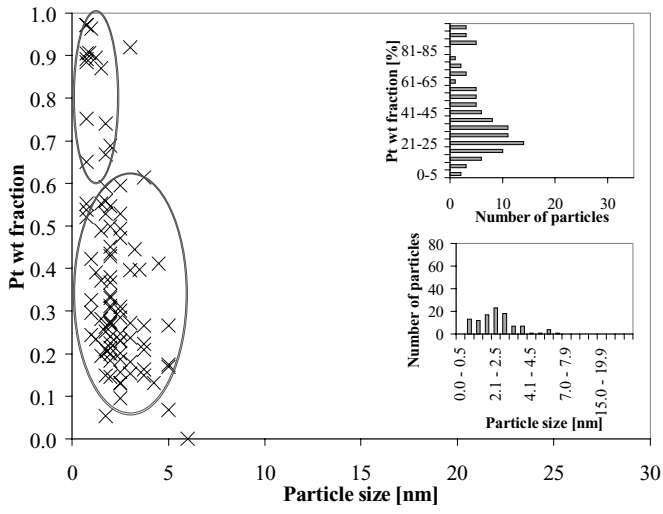

FIG. 4. Metal particle diameter and Pt weight fraction in individual metal particles in sample ALU_F (fresh Pt–Sn catalyst on γ-Al_2O_3 support).

for Pt (9 Pt surface atoms) to obtain 46 at% Pt. A similar procedure was applied to the second method, where we assumed that the metal particles have (fcc) structure. Finally, the number of surface platinum atoms in the particles was counted and the dispersion of each metal particle could be calculated. We refer to this calculated dispersion as "EDX dispersion."

The results for calculated EDX dispersion using specific Pt–Sn phases or (fcc) structure are summarized in Table 2, columns 3 and 4. The EDX dispersions calculated with these two methods are very similar. We assume that the metal particles are more likely to have the (fcc) structure; therefore, we use only EDX dispersion values calculated from the (fcc) structure in this discussion. We did not attempt to identify the crystal structure of the particles on diffraction patterns because of the small metal particle size and low metal loadings. Thus, we do not have evidence for any crystal structure. However, using the (fcc) structure has two advantages: (a) it is simpler and (b) it does not require the tenuous assumption involved with the use of specific compounds from the equilibrium-phase diagram. Moreover, the composition–size diagrams exhibit a smooth distribution of particles across the composition range (Figure 4–9), with no clear discontinuities. This indicates that there are probably

TABLE 2

Comparison of Chemisorption Dispersion Results and EDX Dispersion

Sample	Experimental (from vol. chemisorption)	Calculated from EDX data: Calculated assuming Pt–Sn phases[a]	Calculated from EDX data: (fcc) Structure: Calculated[b]	Calculated for CO[c]	Calculated for CO with support blockage[d]
ALU_F	—	0.43	0.43	—	—
ALU_R	0.35 ± 0.02	0.60	0.56	0.39	0.31 No SMSI
MGO_F	—	0.48	0.50	—	—
MGO_R	0.09 ± 0.02	0.70	0.71	0.50	0.40 SMSI (78%)
HT1_F	—	0.33	0.35	—	—
HT1_R	0.18 ± 0.02	0.69	0.70	0.49	0.39 SMSI (54%)

[a] Metal particles with different crystallographic structures and sizes were generated assuming different Pt–Sn phases (using a phase diagram) according to composition obtained form EDX analysis. Dispersion of each particle was calculated from the total number of Pt atoms and number of surface Pt atoms in the generated particles and corrected by actual composition of the individual particle.

[b] Metal particles with Pt(fcc) structure and different sizes were generated. Dispersion of each metal particle was calculated from the total number of Pt atoms and number of Pt surface atoms in the generated particles and corrected by actual composition of the individual particle.

[c] EDX dispersion recalculated using Fig. 10, which shows that there is 30% less Pt coverage than would be expected from bulk composition (column 5 = column 4 × 0.7).

[d] EDX dispersion recalculated using Fig. 11, which assumes that 20% of the Pt surface atoms do not chemisorb CO because of blockage from the support, and using Fig. 10, which takes into account Sn segregation to the surface (column 6 = column 5 × 0.80). Column 7 indicates strong metal–support interaction (SMSI), with the percentage of Pt surface atoms that do not chemisorb CO in parentheses (column 7 = 100% − column 2/column 6 × 100).

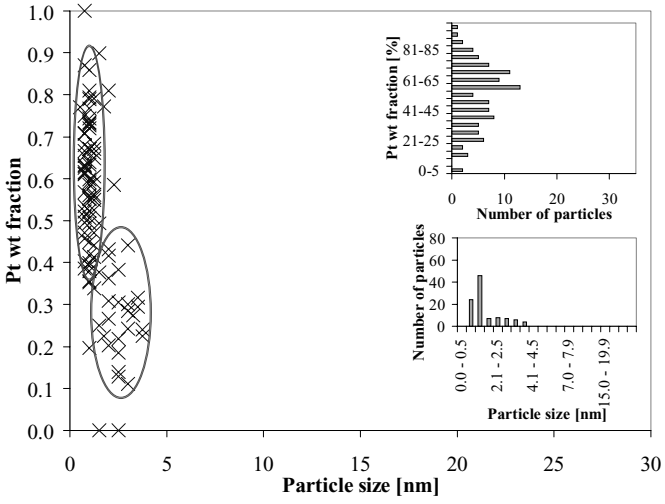

FIG. 5. Metal particle diameter and Pt weight fraction in individual metal particles in sample ALU_R (reduced Pt–Sn catalyst on γ-Al_2O_3 support).

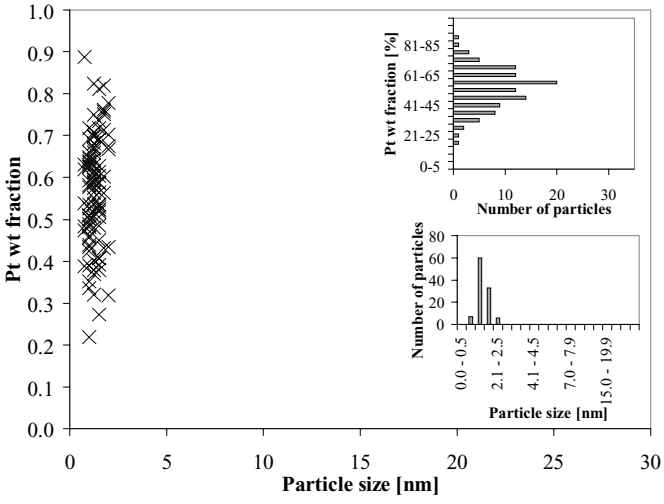

FIG. 7. Metal particle diameter and Pt weight fraction in individual metal particles in sample MGO_R (reduced Pt–Sn catalyst on MgO support).

not different phases present but rather a continuous variation of composition.

The surface composition of a bimetallic particle can differ from its bulk composition. Even after reduction in hydrogen, the Pt : Sn ratio on the surface was found to be lower than in the bulk, which means that the surface is Sn rich (8, 36–38). The equilibrium segregation of Sn to the surface is likely because Sn has a lower surface energy than Pt. The surface and bulk compositions of different Pt–Sn bimetallic samples previously reported (8, 36–38) indicate that the $Pt_{surface} : Pt_{bulk}$ ratio of such samples is about 0.7 (Fig. 10). This means that the chemisorption measurement will indicate less Pt on the surface, leading to lower chemisorption dispersion (larger apparent size of metal particles). We have considered this fact by assuming that there are 30% fewer Pt atoms on the particle surface. Since CO only adsorbs on Pt we recalculated the EDX dispersion (Table 2, column 4) values to obtain predicted EDX dispersion for volumetric chemisorption (Table 2, column 5).

The EDX dispersion for the ALU_R sample is 39%, and the volumetric chemisorption gives a Pt dispersion of 35% (Table 2). While the EDX dispersion is slightly higher, it does not take into account those surface Pt atoms that are inaccessible for CO chemisorption because they are in contact with support (Fig. 11). Estimating from Fig. 11 that

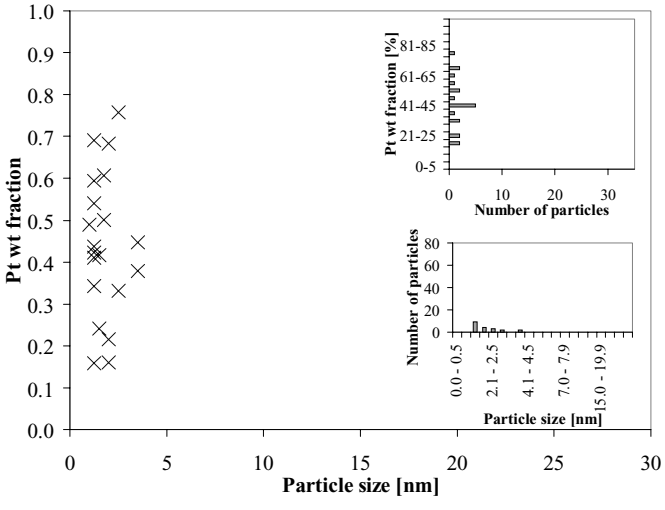

FIG. 6. Metal particle diameter and Pt weight fraction in individual metal particles in sample MGO_F (fresh Pt–Sn catalyst on MgO support). Only a small number of data points was collected because it was difficult to determine the particle boundaries causing a greater error in the metal particle size.

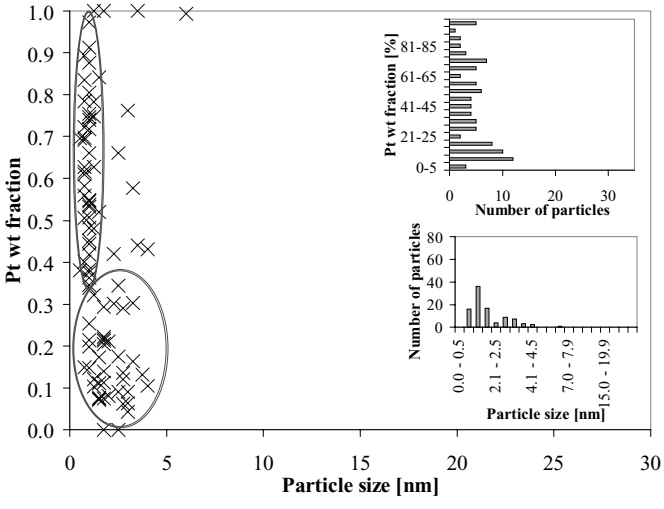

FIG. 8. Metal particle diameter and Pt weight fraction in individual metal particles in sample HT1_F (fresh Pt–Sn catalyst on Mg(Al)O support).

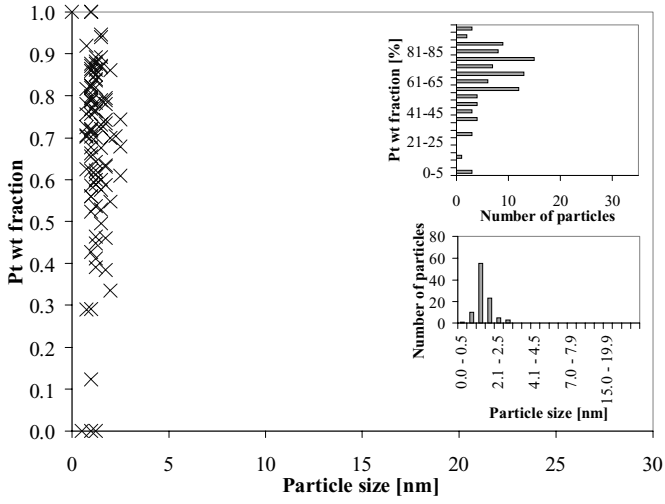

FIG. 9. Metal particle diameter and Pt weight fraction in individual metal particles in sample HT1_R (reduced Pt–Sn catalyst on Mg(Al)O support).

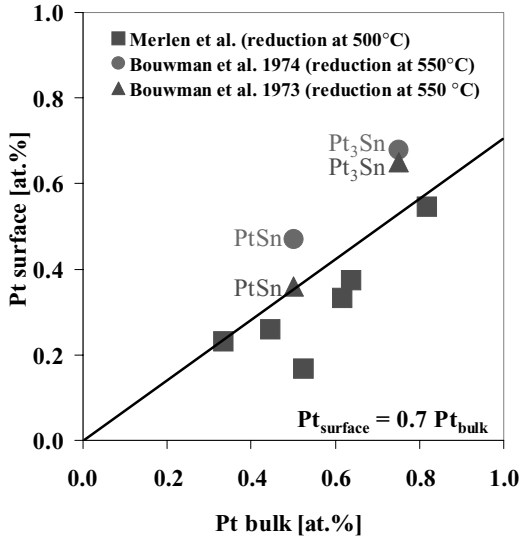

FIG. 10. Concentration of surface platinum atoms on different Pt–Sn intermetallic compounds.

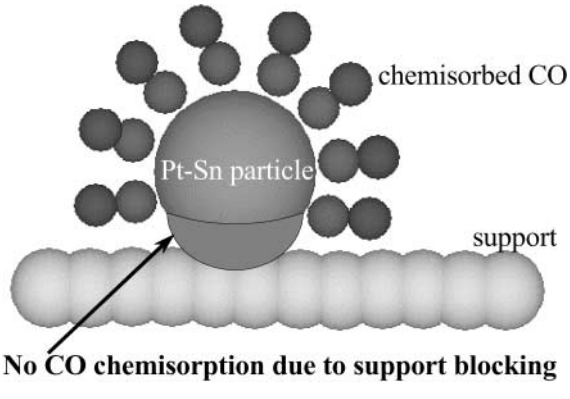

FIG. 11. Blockage of CO chemisorption on Pt–Sn particle caused by the physical contact of the particles and the support.

about 20% of surface Pt atoms are blocked in this way, the final estimated EDX dispersion is reduced to 31% (Table 2, column 6).

Catalyst Activity

Pelletized samples were crushed and sieved to produce particles in the range 0.63–1.00 mm, which were used for catalytic testing. A fixed-bed titanium reactor was loaded with approximately 2 g of catalyst. The catalyst was activated *in situ* by five cycles of reduction in hydrogen at 600°C, a 2-h propane dehydrogenation at 630°C, and regeneration at 600°C by air diluted with nitrogen. The oxygen content was initially 2 mol% and was increased in steps up to 21 mol% (100% air). The last step in pretreatment was reduction in hydrogen at 600°C.

The propane dehydrogenation was performed at a total pressure in the reactor of 1.1 bar and the reaction temperature was 600°C. The weight hourly space velocity (WHSV) during propane dehydrogenation was 4 h^{-1} based on propane, and the reaction mixture contained 4.5 mol% hydrogen, 32.0 mol% propane, and 63.5 mol% steam. The catalysts were tested for 10 h and the products were analyzed with a gas chromatograph equipped with a flame ionization detector (FID) and a thermal conductivity detector (TCD). The samples were regenerated at 600°C by air diluted with nitrogen. The oxygen content was initially 2 mol% and was increased in steps up to 21 mol% (100% air).

RESULTS

STEM/EDX and Volumetric Chemisorption

The results from STEM/EDX are presented in Figs. 4–9. Each point in these composition–size diagrams represents the particle size and Pt weight fraction of a single metal particle. The metal particle size is from the ADF image and the Pt weight fraction in the metal particle is from EDX analysis. The two inset figures (number of particles vs Pt weight fraction; number of particles vs particle size) show more clearly the distribution of values in composition (the upper figure) and particle size (the lower figure). These inset figures allow the reader to distinguish easily single-mode distributions (Fig. 7) from bimodal distributions (Figs. 4 and 5).

The dispersion results from volumetric chemisorption are presented in Table 2, column 2. The next two columns in Table 2 show calculated dispersions from EDX data using either specific Pt–Sn phases (column 3) or (fcc) structure (column 4) according to the composition of the metal particles. We assumed that there are 30% fewer Pt atoms on the particle surface (Fig. 10) and corrected the data to obtain EDX dispersion for CO chemisorption (column 5). After correcting for support occlusion of Pt surface

atoms, the ALU_R sample has a calculated EDX dispersion of 0.31 (column 6), which compares favorably with the 0.35 dispersion from chemisorption (column 2). The MGO_R and HT1_R EDX dispersion still do not compare well with chemisorption and reasons will be given in the discussion.

The EDX dispersion is an averaged dispersion from the individual metal particles measured. Some samples indicate a bimodal distribution of metal particles, in which each group has a characteristic particle size (e.g., Fig. 5) and averaging is not appropriate. Metal particle size distribution and composition on each sample will be presented separately. We stress that the averaging of these data is only for comparison with the chemisorption and activity data.

ALU sample. The composition–size diagram of sample ALU_F (Fig. 4) indicates a phase separation. There appear to be two phases: (a) 0.75–2.00 nm, 60–100 wt% Pt and (b) 0.75–5.00 nm, 0–60 wt% Pt. A characteristic feature of these phases is that the distribution of metal particle sizes and compositions is quite large. The composition of the metal particles changed after reducing the sample (Fig. 5 compared to Fig. 4). There is still an indication of two groups, but as shown in Fig. 5, the metal particles are smaller in both groups and the average Pt content changed slightly as well: (a) 0.75–1.25 nm, 45–90 wt% Pt and (b) 1.00–3.75 nm, 10–45 wt% Pt. Moreover, the number of metal particles in the first group, Pt rich, increased dramatically. If the compositions of all the metal particles were homogeneous and the Pt : Sn ratio was according to nominal metal loading, all the metal particles would contain about 22 wt% Pt (Table 1). However, only about a half of the metal particles on fresh sample have 10–30 wt% Pt and about a fifth on the reduced sample. The rest of the metal particles contained a much higher amount of Pt. We were not able to locate the remaining Sn with STEM/EDX.

MGO sample. The number of visible metal particles on sample MGO_F was high, and the support and metal particles were not easily damaged under the electron beam. However, the images were blurry, and it was difficult to recognize metal particle boundaries. Some Sn was present almost every place on the sample, even when no Sn particles/patches where visible. There were also several spots on which Pt was detected but no metal particle was visible. The composition–size diagram shows that the observable metal particles were in a range of 1.00–3.50 nm (Fig. 6). There is a greater error in the metal particle size, as it was difficult to determine the particle boundaries. Because of that and the very blurry ADF images, only a small number of data points on this sample was collected. Metal particles on this sample contained 15–80 wt% Pt. The number of metal particles across this composition range seemed fairly uniform and formed only one group (one phase).

After reducing the sample, the number of visible metal particles increased dramatically, and the particle boundaries became well-defined (MGO_R). It was the only sample in which metal particles of about 1 nm were also visible in the bright-field image. The composition–size diagram (Fig. 7) shows that the size of the metal particles is between 0.75 and 2.00 nm and particles seem to form only one group, as on the fresh sample. The composition of the metal particles is between 25 and 80 wt% Pt, and the distributions of both composition and size have approximately a Gaussian shape. The greatest number of metal particles is in the range 50–70 wt% Pt. The composition of metal particles is about the same as for sample MGO_F, while the metal particle size appears to have decreased slightly. There is some uncertainty, since we are aware of larger errors in the metal particle size on sample MGO_F. According to the nominal composition measurement, the metal particles on sample MGO_R should have about 44 wt% Pt (Table 1), but it can be seen from the composition–size diagram that the metal particles contain slightly more Pt. We could not locate any Sn-rich particles or patches that would account for the missing Sn.

HT1 sample. The metal particles in the HT1 sample were very difficult to image and analyze for at least the following reasons. First, the support material is highly crystalline and the small crystallites often tend to bend or overlap. Because the crystallites are on the order of a few nanometers, the bending causes strong Bragg diffraction, which tends to look like a metal particle in both bright-field (BF) and annular dark-field (ADF) images. In addition, when single crystals of support overlap, a bright spot is observed in the ADF image that is often indistinguishable from a metal particle. Second, the Mg(Al)O support is much more susceptible to electron beam damage than the γ-Al_2O_3 or MgO supports. Thus, regardless of whether the X-rays were collected when the beam was in spot mode or in scanning mode at 5 Mx, the support material was rapidly destroyed and the metal particle either moved away from the beam, was lost completely, or was buried in a contamination layer such that it could not be recognized after a short analysis time. Third, metal particles smaller than 1 nm were observed occasionally, but they could be analyzed in only a few cases because they disappeared (due to contamination or beam damage) faster than data could be collected. Fourth, metal particles rich in Sn were difficult to locate due to their lower contrast and less visible boundaries.

The fresh sample (HT1_F) seems to have the bimodal distribution: a group of metal particles in the range 0.50–4.00 nm and rich in Sn (0–45 wt% Pt); and a second group of size 0.75–1.50 nm that have a Pt content of 45–100 wt% (Fig. 8). The number of metal particles visible after the reduction increased. Data for approximately the same number of particles were collected, and "visibility" (contrast between metal particles and support) increased as well. The reduction of sample HT1_F also changed the composition of metal particles dramatically. The composition–size diagram

for HT1_R (Fig. 9) shows a group of metal particles with a wide range of composition (30–95 wt% Pt) and a fairly narrow metal particle size range, 0.75–2.50 nm. The Sn-rich group that was present on sample HT1_F disappeared, and the number of Pt-rich particles increased. The composition of metal particles is very different from what would be expected from the bulk Pt : Sn ratio on the sample which was 1 : 4.9 (Table 1). It is not appropriate to calculate a Pt : Sn ratio from the measured distributions. However, it should be noted that the sample contains five times more Sn than Pt, but we detected more Pt-rich particles. The fresh sample had about 40% of its particles containing more than 50 wt% Pt, while the reduced sample had about 85% of such metal particles. This is a larger discrepancy than for the other two samples.

Catalyst Testing

A comparison of catalyst performance at standard operating conditions typical for the propane dehydrogenation process is shown in Fig. 12. The selectivity to propene was close to 90% for all the samples. The initial selectivities to by-products are listed in Fig. 13. The highest conversion of propane is obtained from the HT1_R catalyst and the lowest from the ALU_R catalyst. The catalysts on basic supports (MGO_R, HT1_R) deactivated only slightly over the 10-h dehydrogenation period, with a decrease in activity ((initial activity–final activity)/initial activity) of about 24%. However, the decrease in activity of the ALU_R sample was 54% (Fig. 12).

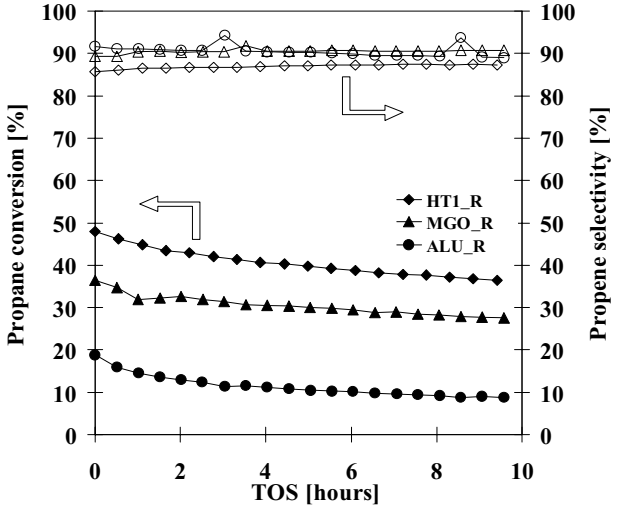

FIG. 12. Propane dehydrogenation as a function of time on stream (WHSV 4 h^{-1}, 1.1 bar, 600°C; feed: 32.5 mol% propane, 4.5 mol% hydrogen, 63 mol% steam). –◆–, HT1_R (0.3 wt% Pt–1.3 wt% Sn/Mg(Al)O); –▲–, MGO_R (1.0 wt% Pt–1.3 wt% Sn/MgO); –●–, ALU_R (0.4 wt% Pt–1.3 wt% Sn/γ-Al_2O_3).

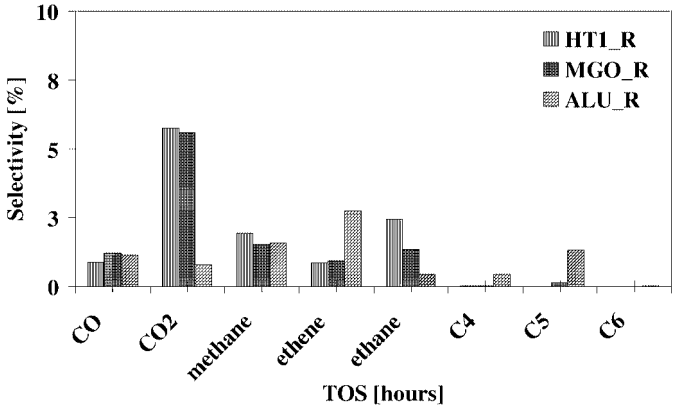

FIG. 13. Initial distribution of by-products in propane dehydrogenation for different catalysts (WHSV 4 h^{-1}, 1.1 bar, 600°C; feed: 32.5 mol% propane, 4.5 mol% hydrogen, 63 mol% steam).

DISCUSSION

Average composition from the particle distributions measured by EDX are presented in Table 1. A majority of the detected particles on all the samples were bimetallic, containing both platinum and tin. It is known that Cl affects the Pt–Sn catalysts (39); thus one could argue that the intimacy between Pt and Sn is caused by the presence of Cl. However, the analysis of samples after preparation indicated very low amount of Cl. Chlorine can also be reliably detected with EDS down to about 0.1–0.5 wt% in a local region. The samples investigated in STEM/EDX did not reveal a Cl peak at 2.4–2.6 keV (Cl K-line) above background (Fig. 1); thus chlorine can only be present in amounts less than 0.1 wt% (under the amount detectable by STEM/EDX). But of course there are caveats. First, the beam can cause a mobile element like Cl to move away from under the beam. Thus, the best chance of detection would be with the shorter collection times. Second, the analysis performed with the STEM/EDX is very localized, and the Cl (if present) may actually reside elsewhere on the support. However, Cl was not detected at short or long collection times on the metal particles and also not on the support. Third, Cl is ubiquitous and has been detected in the STEM from specimens that picked up Cl vapor from the lab environment.

The average Pt content measured in metal particles on the MgO support is close to that introduced by impregnation. However, the Pt content in particles is more than twice nominal content when particles are on γ-Al_2O_3 and Mg(Al)O supports. It is obvious that all the detected metal particles on all the samples contain higher amounts of Pt compared to the nominal loading (Table 1). There are at least two possibile reasons for this observation: (a) part of the Sn evaporated or (b) Sn is spread on the monolayer level over the whole sample and is not generally visible on ADF images. These Sn-rich areas are only visible if the number

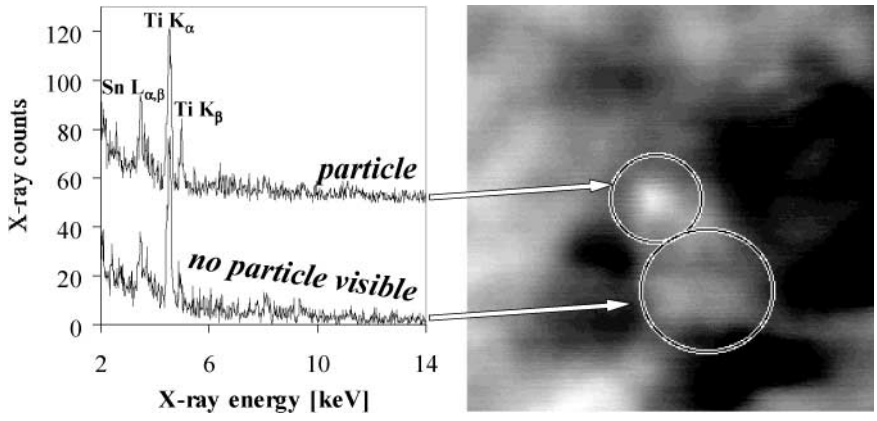

FIG. 14. Example of ADF image with EDX analysis of metal particle and area where no metal particle was visible but Sn was present.

of Sn layers is high enough, and in such cases these areas look like bright patches against darker support material. The latter possibility is supported by the fact that Sn occasionally could be detected on the support in regions with no visible particle (Fig. 14), mainly on the ALU. There is the possibility that electrons scattered from the beam location could excite Sn X-rays from nearby particles; however, in some locations no Sn was found on the support next to Sn-rich particles. The fact that Sn could be spread on the support would agree with Merlen *et al.* (8), who found that bimetallic phases on γ-Al_2O_3 are more easily obtained for larger metal particles than for small ones. In the latter case, the metal particles may be too small to stabilize tin in the metallic state. These authors suggest that tin probably migrates onto the support and remains in an oxidized state in the vicinity of the particle. This is also in agreement with Schwank *et al.* (22), who found tin within close proximity of platinum particles supported on γ-Al_2O_3. They also observed platinum–tin alloy particles in a few instances. However, most of the platinum in their case was present in monometallic form, with some metal particles in intimate contact with patches of ionic tin.

A comparison of fresh and reduced samples (Figs. 4–9) shows that the composition and size of the metal particles changed after reduction. On samples with a bimodal metal particle size distribution (ALU and HT1), the size of Pt-rich particles decreased slightly during reduction, while the size of Sn-rich particles tended to decrease noticeably. Moreover, the number of measured Sn-rich particles was smaller on the reduced samples (ALU_R, HT1_R). Reduction seems to cause Sn migration from the metal particles onto the support, and Sn could spread onto the support in a monolayer (which was not detectable in our experiments). The Sn migration from metal particles during reduction would show on the composition–size diagrams as a decrease in Sn-rich particle size and a shift toward high Pt weight percent in all metal particles.

The method for calculating the dispersion from EDX data (Table 2, column 6) is in good agreement with the experimental chemisorption result (Table 2, column 2) for the ALU_R sample: the EDX dispersion was 0.31 compared to 0.35 obtained from volumetric chemisorption. In contrast, the chemisorption dispersion for the MGO_R sample is only 9%, although the predicted value from EDX data is 40% (Table 2). This means that 78% of surface Pt atoms are unable to chemisorb CO under the conditions used for volumetric chemisorption (Table 2, column 7), and such a large discrepancy cannot be ascribed to partial blockage of Pt surface atoms by the support. Rather it could be caused by a special Pt–O surface interaction, reported by other authors (40–43) on Pt/MgO and by Kazansky and Borovkov (44) on Pt/Mg(Al)O. They suggest that Pt particles, are negatively charged due to electron transfer from basic oxygen anions to the Pt particles, thus preventing donation of the lone pair on carbon to the metal. This may be the reason chemisorption measurements gave a lower dispersion than would be expected from STEM results and activity tests. The total amount of adsorbed CO is not effected dramatically by Sn. However, microcalorimetric studies (45, 46) showed that although the initial differential heat of adsoption is about the same for Pt and Pt–Sn catalysts, the apparent distribution of site strengths for the adsorption of CO on Pt–Sn catalysts is different compared to Pt catalysts. The adsorption sites that adsorb CO most strongly decrease substantially on Pt–Sn catalysts and the highest population of the adsorption sites shifted to lower differential heats (lower site strengths). It was also reported (47–49) earlier that the probe molecule (CO) can be removed by evacuation. The removed molecules could be physically adsorbed and/or not very strongly chemisorbed on Pt. In this study, we suggest that CO was not adsorbed strongly enough on Pt atoms supported on Mg(Al)O and MgO and a 30-min evacuation removed it. We showed that a large percentage of CO can be removed by evacuation (50) on Mg(Al)O samples with

similar EDX dispersion, and that the amount of removed CO depends on the preparation method. We also demonstrated earlier (50) that dispersion calculated from the total amount of adsorbed CO is close to EDX dispersion. The presence of Sn does not have a strong effect on the fraction of CO that is removed (50). It is the support material that influences the adsorption properties of Pt.

Similarly, volumetric chemisorption for the HT1_R sample yields a dispersion of only 18%, while the predicted EDX dispersion is 39% (Table 2, column 2 and 6). This means that 54% of surface Pt atoms are not able to chemisorb CO or chemisorb CO weakly (Table 2, column 7). Thus, the number of Pt surface atoms that chemisorb CO after evacuating the sample is between that for the ALU_R and the MGO_R samples; it is higher than on MgO support but lower than on γ-Al_2O_3. This supports the theory of interaction between Pt and O on MgO-rich supports. The strong metal–support interaction is the weakest on γ-Al_2O_3 support, if it occurs at all, and increases in the order γ-Al_2O_3 < Mg(Al)O < MgO. Furthermore, it is clear that CO chemisorption is not an applicable technique for dispersion measurements of Pt on MgO-rich supports.

The propane conversions and selectivities to propene are presented in Fig. 12. For purposes of comparison, we assumed in Table 3 that the HT1_R catalyst had a relative conversion of 100% and scaled the other conversions for ALU_R and MGO_R catalysts. The catalysts regained their original activity after the regeneration procedure, which indicates that the deactivation was not permanent and that carbon deposition is the main cause of the deactivation.

Catalyst activity is connected with the amount of Pt in the metal particles. The variation in the number of active Pt surface atoms is not due to the change in metal particle size, as all Pt-rich particle diameters were around 1 nm, as shown in the composition–size diagrams. The ALU_R sample contains two groups of metal particles (Fig. 5), and we expect that the second group, larger Sn-rich particles, have very low, if any, activity in propane dehydrogenation. Therefore, we assume that Pt surface atoms in this Sn-rich group have no activity. It was reported by Dong *et al.* (51) that the conversion can decrease over a catalyst with a low Pt : Sn ratio, which presumably consists largely of Sn-rich particles.

TABLE 3

Propane Conversion as a Function of Number of Pt Surface Atoms

	Propane dehydrogenation		STEM/EDX	
Sample	Initial conversion (%)	Relative initial conversion (%)	Pt fraction in the metal particles	Total amount of Pt/g_{cat} (g)
ALU_R	18	35	0.46	0.004
MGO_R	32	63	0.57	0.010
HT1_R	51	100	0.68	0.003

We believe that a certain percentage of Sn in the Pt-rich metal particles is essential to decrease the deactivation rate (53) and that the rest of the Sn should be deposited on the support, preventing sintering of Pt-rich particles (16). It is generally assumed (54) that the rate of carbon formation is comparable on Pt and Pt–Sn catalysts; however, the presence of Sn increases the catalyst stability. Therefore, the most active and stable catalyst would have Pt-rich particles although not pure Pt.

It is very often assumed that it is the total number of Pt surface atoms that is important and that determines the activity of the catalyst. Our samples have fairly similar EDX dispersion (Table 2); thus the conversion should be related to the nominal loading of Pt on the sample. We can see from Table 3 that the MGO_R sample has the highest amount of Pt per gram of catalyst. But it is not the most active catalyst. The sample that gives the highest conversion is the one that has in fact the lowest amount of Pt. That shows clearly that the amount of Pt is not crucial. However, we can see from Table 3 that there is a relationship between the conversion of propane and the fraction of Pt in the metal particles. From Fig. 9 it can be seen that sample HT1_R has the highest population of Pt-rich particles, containing 60–90 wt% Pt. The second highest would be the MGO_R sample, which has metal particles with compositions in the range 45–65 wt% Pt. The ALU_R sample has the lowest number of Pt surface atoms available for propane dehydrogenation because almost half of the Pt surface atoms are present in Sn-rich particles (and thus are not counted as active). The composition–size diagrams and Table 3 show that the conversion increases with increasing amount of Pt in the metal particles. This is very important finding that would not be possible to discover without detailed composition and size of individual metal particles on Pt–Sn catalysts.

The distribution of by-products in Fig. 13 shows that γ-Al_2O_3 support results in more higher hydrocarbons formed by polymerization reactions compared to the MgO and Mg(Al)O supports. The latter catalysts produce more CO_2, which indicates that the supports help to gasify coke.

CONCLUSION

A detailed study of the composition and size of individual Pt–Sn metal particles on γ-Al_2O_3, MgO, and Mg(Al)O has been presented. A method for calculating dispersion from STEM/EDX data for bimetallic catalysts was developed. Dispersion results by this method were in good agreement with those obtained from volumetric chemisorption for Pt–Sn/γ-Al_2O_3. Poor correlation of dispersion results for MgO and Mg(Al)O supports is attributed to interaction between Pt and MgO (strong metal–support interaction). Thus, some platinum surface atoms may adsorb CO weakly and thus CO can be removed during evacuation. STEM/EDX is therefore a suitable method for evaluating

the Pt–Sn catalysts. Metal particles contain more platinum than would be expected from the Pt : Sn ratio that was deposited on the catalyst. Some samples contained at least two groups of metal particles with characteristic size and composition. It was shown that the composition and the size of metal particles can change dramatically after reduction: the metal particle size tends to decrease and Sn-rich particles either disappear or the percentage of them decreases. The conversion of propane correlates well with the Pt fraction in the metal particles. The most active is a catalyst that contains metal particles with high Pt content; however, some Sn is necessary for increased stability.

ACKNOWLEDGMENTS

Statoil and the Norwegian Research Council (NFR) are acknowledged for financial support. The analytical electron microscopy was performed at the Materials Science Center of Lehigh University. We thank Dave Ackland for assistance in the microscope operation. The Mg(Al)O sample was donated by Statoil, which also funded the analytical electron microscopy data collection at Lehigh University.

REFERENCES

1. Cortright, R., and Dumesic, J., *J. Catal.* **158**, 77 (1994).
2. Padró, C. L., de Miguel, S. R., Castro, A. A., and Scelza, A., *Stud. Surf. Sci. Catal.* **119**, 191 (1998).
3. Siri, G. J., Casella, M. L., Santori, G. F., and Ferretti, O. A., *Ind. Eng. Chem. Res.* **36**, 4821 (1997).
4. Rebo, H. P., Chen, D., Blekkan, E. A., and Holmen, A., *Stud. Surf. Sci. Catal.* **119**, 617 (1998).
5. Bariås, O. A., Holmen, A., and Blekkan, E. A., *J. Catal.* **158**, 1 (1996).
6. Vázquez-Zavala, A., Ostoa-Montes, A., Acosta, D., and Gómez-Cortés, A., *Appl. Surf. Sci.* **136**, 62 (1998).
7. Burch, R., *J. Catal.* **71**, 348 (1981).
8. Merlen, E., Beccat, P., Bertolini, J. C., Delichère, P., Zanier, N., and Didillon, B., *J. Catal.* **159**, 178 (1996).
9. Passos, F. B., Aranda, D. A. G., and Schmal, M., *J. Catal.* **178**(2), 478 (1998).
10. Huang, Z., Fryer, J. R., Park, C., Stirling, D., and Webb, G., *J. Catal.* **159**, 340 (1996).
11. Rajashwer, D., Basrur, A. G., Gokak, D. T., and Krishnamurthy, K. R., *J. Catal.* **150**, 135 (1994).
12. Chojnacki, T. P., and Schmidt, L. D., *J. Catal.* **129**, 473 (1991).
13. Moroz, E. M., Pakhomov, N. A., Kotelnikov, G. R., Buyanov, R. A., and Patanov, V. A., *React. Kinet. Catal. Lett.* **7**(4), 457 (1977).
14. Biloen, P., Dautzenberg, F. M., and Sachtler, W. M. H., *J. Catal.* **50**, 77 (1977).
15. Armendáriz, H., Guzman, A., Toledo, J. A., Llanos, M. E., Vazquez, A., and Aguilar-Ríos, G., *Appl. Catal. A* **211**(1), 69 (2001).
16. Llorca, J., Homs, N., León, J., Sales, J., Fierro, J. L. G., and Ramires de la Pscina, P., *Appl. Catal. A* **189**, 77 (1999).
17. Aguilar-Ríos, G., Salas, P., Valenzuela, M. A., Armendáriz, H., and Wang, J. A., *Catal. Lett.* **60**(1, 2), 21 (1999).
18. Cavani, F., and Trifirò, F., *Chim. Ind.* **76**(11), 708 (1994).
19. Hansen, T. W., Wagner, J. B., Hansen, P. L., Dahl, S. Topsøe, H., and Jacobsen, C. J. H., *Science* **294**, 1508 (2001).
20. Prestvik, R., Tøtdal, B., Lyman, C. E., and Holmen, A., *J. Catal.* **176**, 246 (1998).
21. Lakis, R. E., Lyman, C. E., and Stenger, H. G., *J. Catal.* **154**, 261 (1995).
22. Schwank, J., Balakrishnan, K., and Sachdev, A., *Stud. Surf. Sci. Catal.* **75**, 905 (1993).
23. Mériaudeau, P., Naccache, C., Thangaraj, A., Bianchi, C. L., Carli, R., Vishvanathan, V., and Narayanan, S., *J. Catal.* **154**, 345 (1995).
24. Srinivasan, E., Sharma, R., Su, S., and Davis, B. H., *Catal. Today* **21**, 83 (1994).
25. Akporiaye, D., Rønnekleiv, M., and Hasselgård, P., U.S. Patent 5,817,596 (1994).
26. Akporiaye, D., Jensen, S. F., Olsbye, U., Rohr, F., Rytter, E., Rønnekleiv, M., and Spjelkavik, A. I., *Ind. Eng. Chem. Res.* **40**, 4741 (2001).
27. Olsbye, U., Akporiaye, D., Rytter, E., Rønnekleiv, M., and Tangstad, E., *Appl. Catal.* **224**, 37 (2002).
28. Lyman, C. E., Goldstein, J. I., Williams, D. B., Ackland, D. W., Von Harrach, S., Nicholls, A. W., and Statham, P. J., *J. Microsc. (Oxford)* **176**(2), 85 (1994).
29. Williams, D. B., and Carter, C. B., "Transmission Electron Microscopy, Spectroscopy IV." Plenum, New York, 1996.
30. Fiori, C. E., Swyt, C. R., and Myklebust, R. L., U.S. Patent 5,299,138 (1992).
31. Cliff, G., and Lorimer, G. W., *J. Microsc.* **103**, 203 (1975).
32. Goldstein, J. I., Costley, J. L., Lorimer, G. W., and Reed, S. J. B., *SEM 1977* **1**, 315 (1977).
33. Wood, J. E., Williams, D. B., and Goldstein, J. I., *J. Microsc.* **133**(3), 255 (1984).
34. Ravel, B., "WebATOMS Version 1.4." University of Washington, Seattle, 2000.
35. Lloyd, L. D., and Johnston, R. L., *J. Chem. Soc. Dalton Trans.* 307 (2000) and http://www.tc.bham.ac.uk/bcweb/M17-19/.
36. Asbury, D. A., and Hoflund, G. B., *Surf. Sci.* **199**, 552 (1988).
37. Bouwman, R., and Biloen, P., *Anal. Chem.* **46**(1), 136 (1974).
38. Bouwman, R., Toneman, L. H., and Holscher, A. A., *Surf. Sci.* **35**, 8 (1973).
39. Arteaga, G. J., Anderson, J. A., and Rochester, C. H., *J. Catal.* **187**, 219 (1999).
40. Adamiec, J., Wanke, S. E., Tesche, B., and Klengler, U., *Stud. Surf. Sci. Catal.* **11**, 77 (1982).
41. Clarke, J. K. A., Bradley, M. J., Garvie, L. A. J., Craven, A. J., and Baird, T., *J. Catal.* **143**, 122 (1993).
42. Recchia, S., Dossi, C., Poli, N., Fusi, A., Sordelli, L., and Psaro, R., *J. Catal.* **184**, 1 (1999).
43. Goldwasser, J., Bolivar, C., Ruiz, C. R., Arenas, B., Wanke, S., Royo, H., Barrios, R., and Giron, J., *in* "Proceedings, 8th International Congress on Catalysis, Berlin, 1984," p. 195. Dechema, Frankfurt-am-main, 1984.
44. Kazansky, V. B., and Borovkov, V. Yu., *Catal. Lett.* **19**, 327 (1993).
45. Cortright, R. D., and Dumesic, J. A., *J. Catal.* **148**, 771 (1994).
46. Jia, J., Lin, L., Shen, J., Xu, Z., Zhang, T., Liang, D., and Chen, Y., *Sci. China Ser. B* **41**(6), 606 (1998).
47. Palmer, M. B., Jr., and Vannice, M. A., *J. Chem. Tech. Biotechnol.* **30**, 205 (1980).
48. Dorling, T. A., and Moss, R. L., *J. Catal.* **5**, 111 (1966).
49. Eischens, R. P., and Pliskin, W. A., *Adv. Catal.* **10**, 1 (1958).
50. Bednarova, L., Ph.D. dissertation. NTNU, Trondheim, Norway, 2002.
51. Dong, W., Wang, H., Wang, X., and Peng, S., *Tianranqi Huagong* **24**(3), 9 (1999).
52. Watwe, R. M., Cortright, R. D., Mavrikakis, M., Nørskov, J. K., and Dumesic, J. A., *J. Chem. Phys.* **114**(10), 4663 (2001).
53. Larsson, M., Andersson, B., Bariås, O. A., and Holmen, A., *Stud. Surf. Sci. Catal.* **88**, 233 (1994).
54. Rebo, H. P., Blekkan, E. A., Bednarova, L., and Holmen, A., *Stud. Surf. Sci. Catal.* **126**, 333 (1999).